

Influence of damping parameters within a finite element model using the example of high energy impacts resulting from dynamic compaction

S Klemm CDM Smith, Germany

A Muehl CDM Smith, Germany

Y Koitzsch CDM Smith, Germany

F Gneist MIBRAG, Germany

Abstract

MIBRAG has planned a new mass distributor on a dump area for the extension of the Vereinigtes Schleenhain open pit mining area in Germany. This plan calls for densification by dynamic compaction to improve the bearing capacity of the in situ dump material. The densification is bordering on an outer slope and it was necessary to guarantee slope stability under the influence of high energy impacts that result from dynamic compaction. For this reason slope stability was analysed using constitutive models in conjunction with a hardening soil model employing small strain stiffness and hysteretic damping. This work included a study of the influence of all parameters that affect soil damping. For this purpose, a finite element (FE) model was used for calibrating the damping parameters with the aim to obtain a reasonable match of calculation results to measured field data. This paper will provide an outline of the project, present the findings of our study on the influence of damping parameters within the FE model and will give an overview of the analysis of slope stability under dynamic compaction.

1 Introduction

MIBRAG produces brown coal in a central Germany coal basin near Leipzig. It owns and operates two surface mines, Profen and Vereinigtes Schleenhain, with a total annual coal production of more than 20 million tonnes. Proven reserves amount to approximately 500 million tonnes of coal, with a significant opportunity for extending extraction because industrial reserves are estimated at two billion tonnes. The Profen mine supplies coal to the Schkopau power station. Vereinigtes Schleenhain supplies its coal to the Lippendorf CHP plant, which holds an over 60% share in district heating in Leipzig. MIBRAG in Germany also owns two CHP plants at Deuben and Wühlitz with an aggregate installed capacity of 123 MW.

MIBRAG planned to build a mass distributor on a dump area in connection with expansion of the working area at the Vereinigtes Schleenhain open pit mine. The mass distributor is a fully automated system which sorts the extracted brown coal and the overburden on different conveyor belts. Brown coal is then transported to a central coal stockyard, while overburden is transported to the dump area.

In order to improve the bearing capacity of the existing dump materials densification using dynamic compaction of the ground by lifting and dropping heavy weights was planned. The area to be improved was within the lower levels of the open pit mine between an outer slope directly bordering on the north side approximately 20 m high and an inner slope in the south approximately 50 m away. The target densification site is shown in plan in Figure 1. The approach used to assess the efficacy of dynamic compaction was to use finite element modelling to discover whether the dynamic effects from falling weight had a negative impacts (such as instability) on the stability of the natural and dumped slopes.

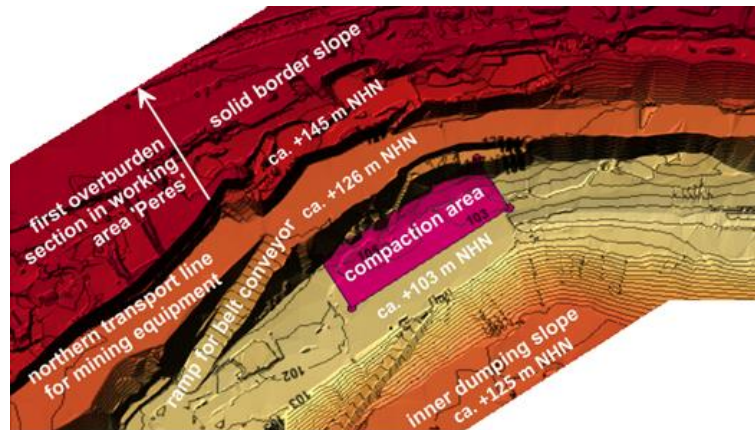


Figure 1 3D ground relief pinpointing outer slope, inner dumping slope and densification site

Slopes were comprised of both natural soils and dumped materials. The inner dumping slope and the majority of the densification site consisted of dumped material to varying depths. The dump thickness, shown in grey in Figure 2, is more than 25 m at the falling weight target densification site which is also identified in Figure 2. However, the dump thickness reduces to approximately 12 m or less towards the upper outer slopes. The groundwater depth is 10 m under the ground at the area to be densified.

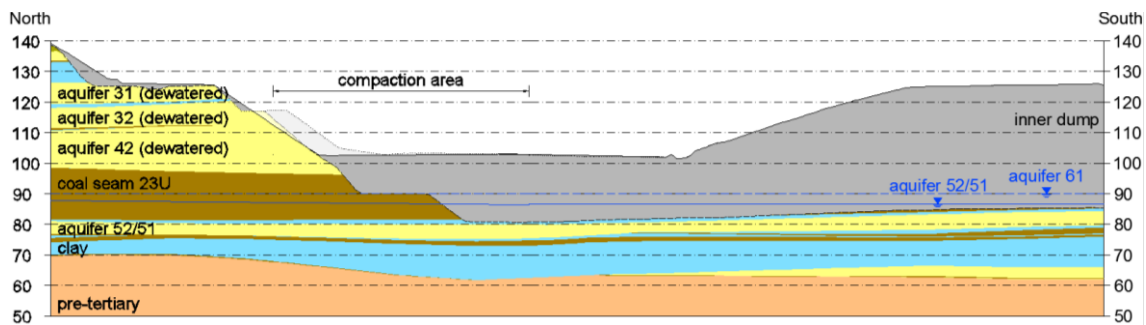


Figure 2 Geotechnical situation in the area of the site planned for the Peres Mass Distributor

The succession of dumped materials at the site has resulted in a very heterogeneous structure including areas of both fine-grained and coarse-grained material. Cone penetration tests in the dumped material showed relatively chaotic interbedded strata in terms of fine-grained and coarse-grained regions, although horizontal or vertical stratification is not recognisable. Furthermore, the coarse-grained dumping zones have predominantly loose layering primarily consisting of fine sand sized material. The dynamic compaction campaign was undertaken by Ecosoil Ost GmbH and comprised approximately 3,890 impact locations (refer to Figure 3 and Table 1).



Figure 3 Compaction field

Table 1 Dynamic compaction

| | |
|------------------------------------|------------------------------------|
| Area to be compacted | 233 × 74 m = 17,242 m ² |
| Impact locations | 3,890 |
| Dimensions of the falling weight | 2 × 2 m |
| Weight | 20 tonnes |
| Compaction grid | 3 × 3 m |
| Impacts per point | 4 |
| Number of rounds | 2 |
| Height of strokes (soil-dependent) | 15/25 m |
| Energy registered | 300/500 tm |
| Registered impulses | 343,103/442,945 Ns |

2 Dynamic modelling/stability tests

2.1 The calculation procedure

Calculations were made based on finite element analyses applying the PLAXIS 2D program. The PLAXIS dynamic module was used to apply the time integration method to analyse the propagation of waves through the soil and their impact on slope stability. The time integration method breaks down the dynamic signal into a defined number of small time steps (time increments) and then resulted stress is calculated for each time increment using the results of the previous time increment (displacement, velocity and acceleration) as the initial input value. This allows the user to analyse the stress state at each time increment which can be presented in compound form, such as extracting all time increments into a sequential recording (video) for example.

To determine the Factor of Safety for slope stability, dynamic calculations were repeated while reducing effective shear strength until a continuous sliding surface, characterising a slope failure could be observed. The Factor of Safety η for the slope was determined with Equation (1) by the ratio of shear strength at failure ($\tan \varphi_{failure}$ respectively $c_{failure}$) to the available shear strength ($\tan \varphi_{input}$ respectively c_{input}) using Fellenius's law (Fellenius 1936).

$$\eta = \frac{\tan \varphi_{input}}{\tan \varphi_{failure}} = \frac{c_{input}}{c_{failure}} \quad (1)$$

2.2 Applying the hardening soil model with the small-strain stiffness model and hysteretic damping

Soils have been modelled using the hardening soil (HS) model with small strain stiffness (HS small model). The HS small model is based on the HS model (Schanz 1999), extended with an elastic overlay model to take into account the high stiffness at small strain levels (Benz 2007; Benz et al. 2006). The HS small model implemented in PLAXIS considers a high stiffness at small strain levels due to the following modulus reduction curve equation:

$$G_S = \frac{G_0}{1 + \frac{a \cdot \gamma}{\gamma_{0.7}}} \quad (2)$$

where: G_S is the secant shear modulus, G_0 is the initial or very small strain shear modulus and $\gamma_{0.7}$ is the shear strain at which the secant shear modulus has reduced to about 70% of G_0 . The constant, a , is given a

value of 0.385 (Plaxis 2015). In the HS small model, the very small strain shear modulus G_0 has a stress dependency, formulated due to:

$$G_0 = G_0^{ref} \left(\frac{c' \cdot \cot \varphi' + \sigma_3'}{c' \cdot \cot \varphi' + p^{ref}} \right)^m \quad (3)$$

The threshold shear strain $\gamma_{0.7}$ is taken independently of the principle stress. It can be defined by using the Mohr–Coulomb failure criterion in Equation (4). For cohesive soils the correlation of Darendeli (2001) can also be used to estimate $\gamma_{0.7}$.

$$\gamma_{0.7} = \frac{1}{9G_0^{ref}} \cdot [2c'(1 + \cos(2\varphi')) - \sigma_1'(1 + K_0) \sin(2\varphi')] \quad (4)$$

The HS small model incorporates hysteretic damping within cyclic loading. The damping ratio ξ can be defined by the ratio of the energy dissipated in a load cycle E_D to the energy stored at the maximum strain of a load cycle E_S :

$$\xi = \frac{E_D}{4\pi E_S} \quad (5)$$

E_D and E_S are defined with Equations (6) and (7).

$$E_D = \frac{4G_0\gamma_{0.7}}{a} \cdot \left(2\gamma_c - \frac{\gamma_c}{1 + \gamma_{0.7}/a\gamma_c} - \frac{2\gamma_{0.7}}{a} \ln \left(1 + \frac{a\gamma_c}{\gamma_{0.7}} \right) \right) \quad (6)$$

$$E_S = \frac{G_0\gamma_c^2}{2 + 2a\gamma_c/\gamma_{0.7}} \quad (7)$$

The magnitude of the cyclic shear strain in which the hysteretic damping exists is defined by:

$$\gamma_c \leq \frac{\gamma_{0.7}}{a} \cdot \left(\sqrt{\frac{G_0}{G_{ur}}} - 1 \right) \quad (8)$$

where: G_{ur} is the shear modulus in unloading/reloading which is defined by stiffness and Poisson's ratio in unloading/reloading in the HS model.

$$G_{ur} = \frac{E_{ur}}{2 \cdot (1 + \nu_{ur})} \quad (9)$$

Brinkgreve et al. (2007) give an extended overview of the derivation of the hysteretic damping from the small-strain stiffness formulation in the HS small model. In this reference the dependency of the damping ratio from $\gamma_{0.7}$ and the G_0/G_{ur} ratio is shown varying $\gamma_{0.7}$ between $1 \cdot 10^{-4}$ to $3 \cdot 10^{-4}$ and the G_0/G_{ur} between 2.5 and 10. Decreasing the value of $\gamma_{0.7}$ makes the material damping increase and even increasing the ratio of G_0/G_{ur} (adequate to E_0/E_{ur}) results in an increase of material damping. From the formulation of the HS small model it can be derived that no more damping occurs as soon as the tangent shear modulus G_t reaches G_{ur} .

$$G_t = \frac{G_0}{\left(1 + \frac{a \cdot \gamma}{\gamma_{0.7}} \right)^2} \geq G_{ur} \quad (10)$$

Figure 4 shows the curve of the tangent shear modulus and the curve of the damping ratio of the dumped material as a function of shear strain. Table 2 shows the related parameter set. The stiffness of the material (HS model) was varied in a range of +/- 50%. The ratio of stiffness in unloading/reloading E_{ur} to stiffness in primary loading E_{50} was held constant with 4. G_0 was determined by using the correlations between very small stiffness and stiffness at large strains after Alpan (1970). $\gamma_{0.7}$ was determined by using the correlation (3).

Table 2 HS small model data set for the dumped material

| Parameter | Symbol | Dumped material | | | Unit |
|---|--------------------------|---------------------|---------------------|---------------------|----------------------|
| | | Lower limit | Average | Upper limit | |
| Unsaturated unit weight | γ_{unsat} | 18.5 | 18.5 | 18.5 | (kN/m ³) |
| Saturated unit weight | γ_{sat} | 20.0 | 20.0 | 20.0 | (kN/m ³) |
| Cohesion | c | 10 | 10 | 10 | (kN/m ²) |
| Friction angle | φ | 22 | 22 | 22 | (°) |
| Stress ratio in primary compression | K_0^{NC} | 0.625 | 0.625 | 0.625 | (-) |
| Reference pressure | p^{ref} | 100 | 100 | 100 | (kN/m ²) |
| Rate of stress-dependency | m | 0.5 | 0.5 | 0.5 | (-) |
| Poisson's ratio for unloading/reloading | ν | 0.2 | 0.2 | 0.2 | (-) |
| Primary oedometer stiffness | E_{oed}^{ref} | 3 | 6 | 9 | (MN/m ²) |
| Triaxial compression stiffness | E_{50}^{ref} | 3 | 6 | 9 | (MN/m ²) |
| Unloading/reloading stiffness | E_{ur}^{ref} | 14 | 24 | 36 | (MN/m ²) |
| Reference shear modulus at very small strains | G_{ur}^{ref} | 5 | 10 | 15 | (MN/m ²) |
| Reference shear modulus at very small strains | G_0^{ref} | 35 | 50 | 70 | (MN/m ²) |
| Ratio G_0^{ref}/G_{ur}^{ref} (after Alpan 1970) | G_0^{ref}/G_{ur}^{ref} | 7.0 | 5.0 | 4.5 | (MN/m ²) |
| Shear strain at which is $G_S = 0.722 \cdot G_0$ | $\gamma_{0.7}$ | $4.7 \cdot 10^{-4}$ | $3.3 \cdot 10^{-4}$ | $2.3 \cdot 10^{-4}$ | (-) |
| Magnitude of the cyclic shear strain with damping | γ_c | $2.0 \cdot 10^{-3}$ | $1.1 \cdot 10^{-3}$ | $7.1 \cdot 10^{-4}$ | (-) |
| Dissipated energy in a load cycle | E_D | 0.066 | 0.026 | 0.016 | (kN/m ²) |
| Energy stored at maximum shear strain γ_c | E_S | 0.026 | 0.012 | 0.008 | (kN/m ²) |
| Maximum damping ratio (at maximum shear strain γ_c) | ξ | 20.0 | 16.7 | 16.0 | (%) |

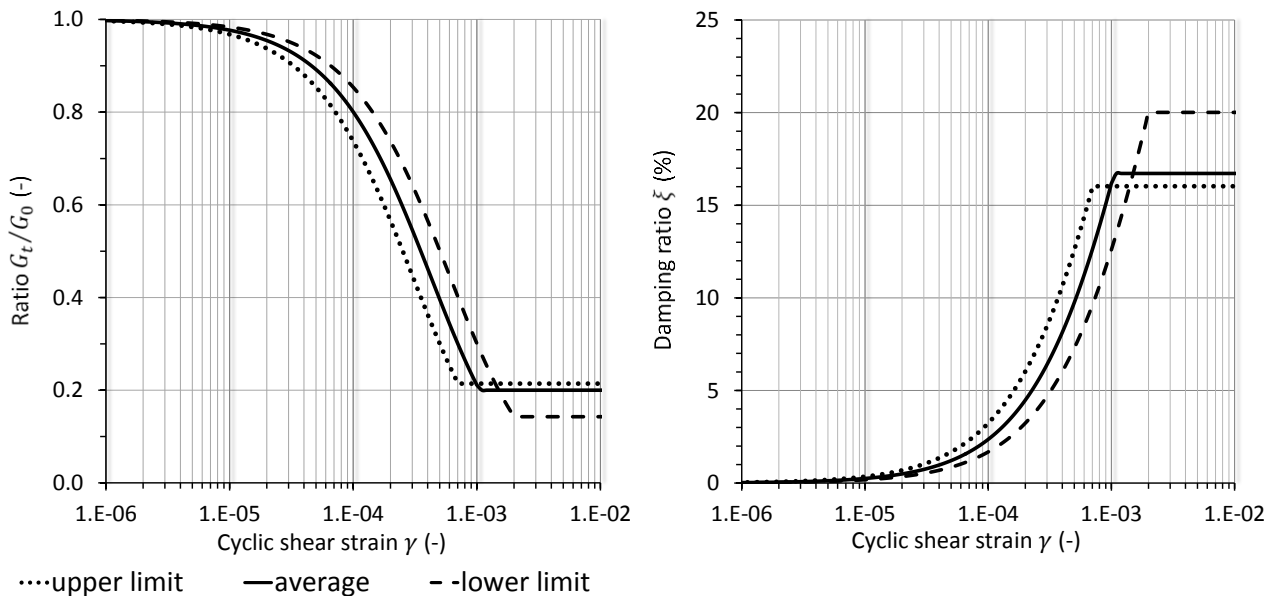


Figure 4 Dumped material, ratio G_t/G_0 and damping ratio ξ as a function of shear strain

2.3 Modelling dynamic compaction

Dynamic compaction can be described as a continuous and selective shot of impulses at greater intervals in terms of dynamic effects. Each shot of impulses generates vibrations that propagate in the loose soil in the form of compression, shear and Rayleigh waves as per Figure 5. After Woods (1968), the portion of Rayleigh waves on the whole amount of energy is 67%, while shear waves constitute 26% and compression waves constitute 7%.

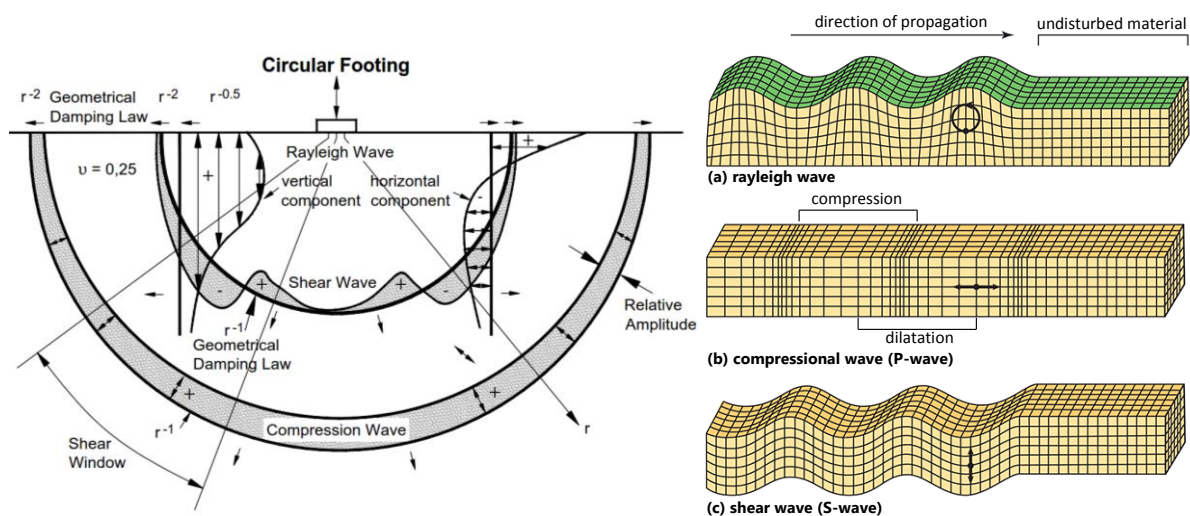


Figure 5 Wave propagation with dynamic point load including the direction of movement (modified from Woods 1968 and Peterie et al. 2014)

The wave amplitudes die out the greater the distance to the entry point due to the soil's damping properties. This damping effect is relatively high in the unimproved soil in the initial stages of dynamic compaction. In the final stages of treatment the damping effect is lower and therefore relative stiffness increases.

A simplified two-dimensional model was used for model calibration of propagation of shear and compression waves resulting from dynamic compaction (refer to Figure 6). The impact point of the falling weight was modelled with an element cluster two metres wide and one metre high. This cluster was bound with interface elements of low stiffness to enable the falling weight to penetrate into the model subsoil. Finally, a dynamic load was generated in the model above the falling weight for simulating the impact impulse.

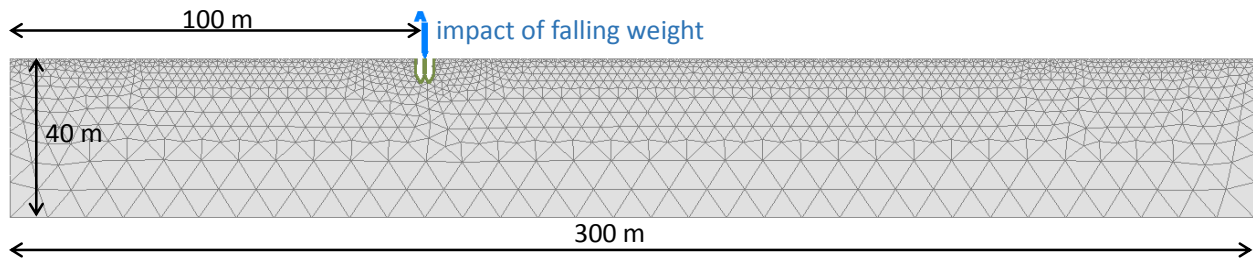


Figure 6 The model for calculating calibration

Geophysik GGD (2010) provided the readings for propagating vibrations in the dumping floor to be studied. However, they applied to densification with an impact impulse of 200 tm. Kirstein and Krings (2012) gives the indicators for the maximum vibration velocity at a compression with an impact impulse of 300 tm and 520 tm (refer to Figure 7).

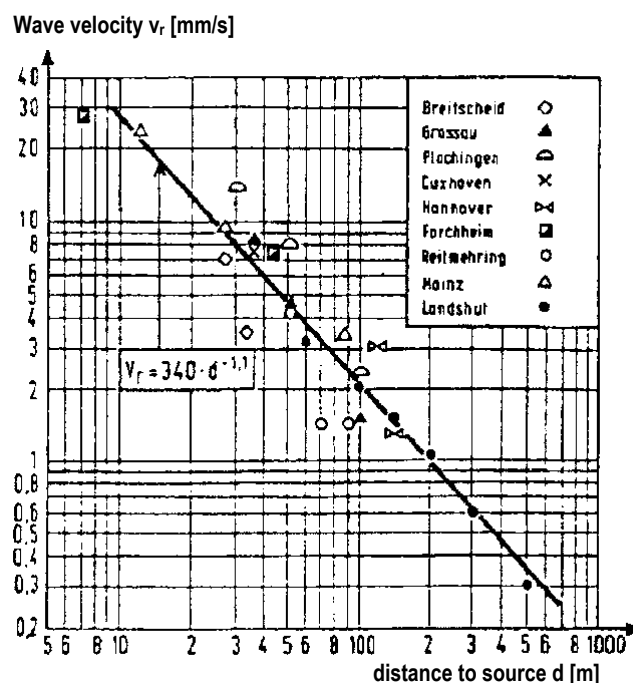


Figure 7 The spread of the vibration velocity depending upon the distance from the dynamic compaction point of impact (300 tm of falling energy), (modified from Kirstein & Krings 2012)

Figure 7 is based on the supposition that the wave velocity given in Geophysik GGD (2010) and Kirstein and Krings (2012) are the maximum of the series of measurements, although their damping capability is reduced due to the soil compression. Model calibration using these wave velocities included the transitional decrease in damping by dynamic compaction over time.

The dynamic load was modelled as a harmonic wave with the parameters of frequency, phase displacement and maximum amplitude. The wave velocities were monitored at observation points at different distances from the impact point of the falling weight under varying parameters and the readings were compared with one another and with the measurement data from Geophysik GGD (2010) and Kirstein and Krings (2012), as shown in Figure 8. It became apparent from this comparison that it was not possible to achieve any sufficient reduction in wave velocity in initially distant areas with the assumptions made in the model (refer to Figure 8). Therefore, it can be concluded that model damping is not high enough in areas with small strains. There is also damping in soils even if strains are very small. This effects are essentially caused due to Rayleigh damping.

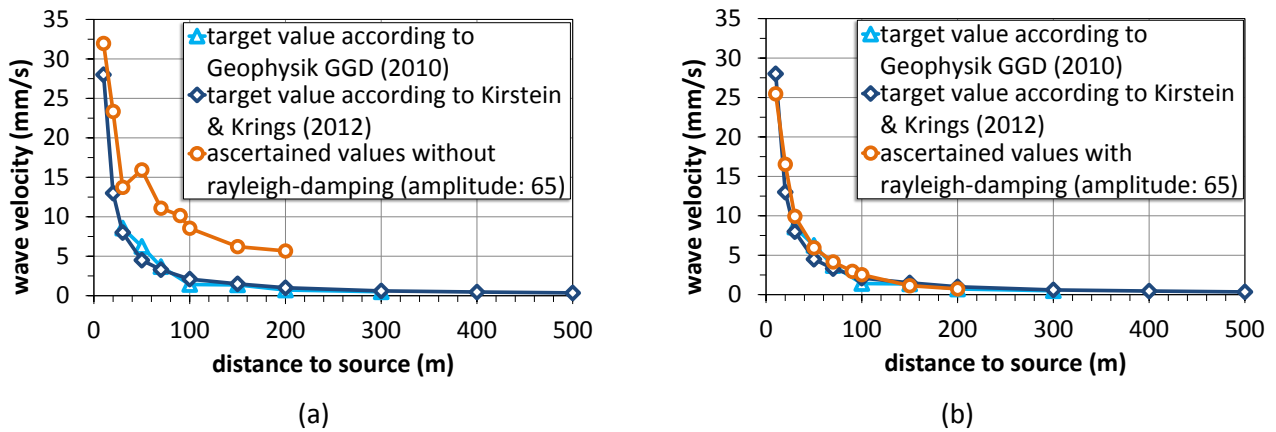


Figure 8 Comparison of the calculated horizontal wave velocity with readings according to Geophysik GGD (2010) and Kirstein and Krings (2012): (a) without using rayleigh-damping; (b) with using rayleigh-damping

The degree of damping ξ was set to be a constant 5%. Then, the key frequency range was varied until sufficient agreement could be achieved with the readings according to Geophysik GGD (2010) and Kirstein and Krings (2012). The laws of Rayleigh damping indicate that there is increasing damping in the model (refer to Figure 9) when the frequency range is decreased. In other words, a 5 Hz difference in Rayleigh frequencies was calculated with reference to this assignment as a key factor for deriving any damping parameters that approximate reality.

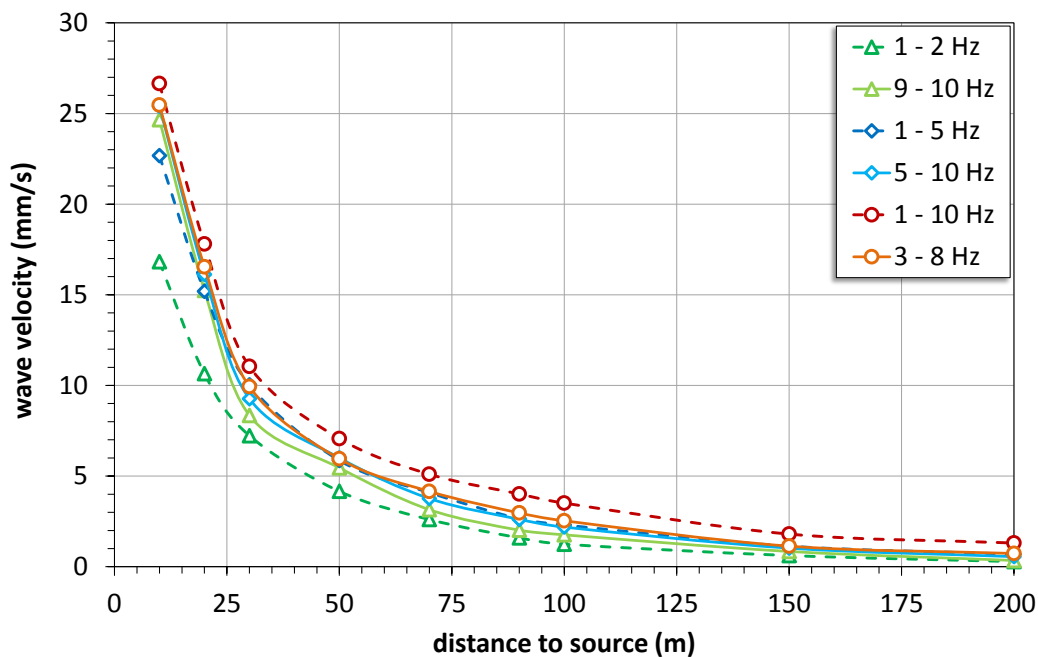


Figure 9 Generated horizontal wave velocity by postulating Rayleigh damping parameters ($\alpha = 1.371$ and $\beta = 1.447 \times 10^{-3}$)

2.4 Slope stability analysis

The model shown in Figure 10 was used for the stability analyses of the outer slope subject to dynamic compaction. The outer slope is 46 m high, but there is a berm with a width of 30 m in the middle of the slope. The inclination of both parts of the slope is about 1:1.5. For dumped material the calibrated HS small model was used in the finite element (FE) model. The parameters used for natural soils are shown in Table 3.

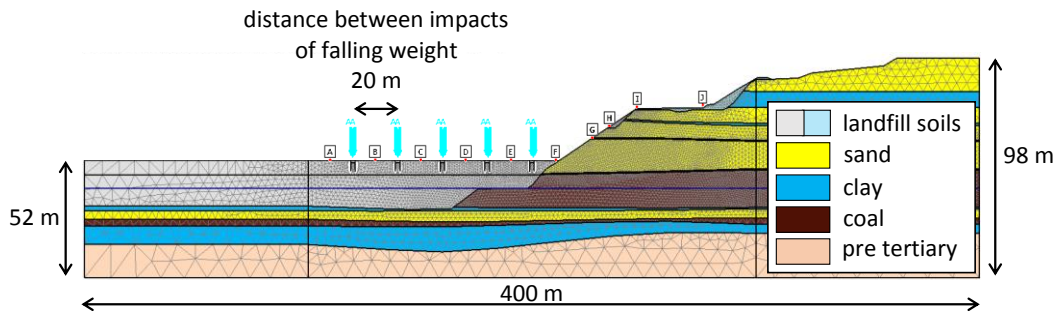


Figure 10 The FE model for studying the effects of dynamic compaction on the solid border slope

Table 3 HS small model data set for natural soils (sand, clay, coal and pre tertiary)

| Parameter | Symbol | Sand | Clay | Coal | Pre tert. | Unit |
|---|--------------------------|---------------------|---------------------|---------------------|---------------------|----------------------|
| Unsaturated unit weight | γ_{unsat} | 19.0 | 20.2 | 11.5 | 20.0 | (kN/m ³) |
| Saturated unit weight | γ_{sat} | 20.0 | 20.2 | 13.0 | 21.0 | (kN/m ³) |
| Cohesion | c | 11 | 26 | 19 | 15 | (kN/m ²) |
| Friction angle | ϕ | 32 | 17 | 32 | 32 | (°) |
| Stress ratio in primary compression | K_0^{NC} | 0.470 | 0.708 | 0.470 | 0.470 | (-) |
| Reference pressure | p^{ref} | 100 | 100 | 100 | 100 | (kN/m ²) |
| Rate of stress-dependency | m | 0.5 | 1 | 0.6 | 0.2 | (-) |
| Poisson's ratio for unloading/reloading | ν | 0.2 | 0.2 | 0.2 | 0.2 | (-) |
| Primary oedometer stiffness | E_{oed}^{ref} | 25.0 | 9.0 | 16.6 | 75.0 | (MN/m ²) |
| Triaxial compression stiffness | E_{50}^{ref} | 25.0 | 5.0 | 16.6 | 75.0 | (MN/m ²) |
| Unloading/reloading stiffness | E_{ur}^{ref} | 75.0 | 25.0 | 50.0 | 150.0 | (MN/m ²) |
| Reference shear modulus at very small strains | G_{ur}^{ref} | 31.0 | 10.0 | 21.0 | 63.0 | (MN/m ²) |
| Reference shear modulus at very small strains | G_0^{ref} | 109.0 | 54.0 | 79.9 | 106.0 | (MN/m ²) |
| Ratio G_0^{ref}/G_{ur}^{ref} (after Alpan 1970) | G_0^{ref}/G_{ur}^{ref} | 3.5 | 5.2 | 3.8 | 1.7 | (MN/m ²) |
| Shear strain which is $G_S = 0.722 \cdot G_0$ | $\gamma_{0.7}$ | $1.7 \cdot 10^{-4}$ | $3.9 \cdot 10^{-4}$ | $2.6 \cdot 10^{-4}$ | $1.8 \cdot 10^{-4}$ | (-) |
| Magnitude of the cyclic shear strain with damping | γ_c | $3.8 \cdot 10^{-4}$ | $1.3 \cdot 10^{-3}$ | $6.5 \cdot 10^{-4}$ | $1.4 \cdot 10^{-4}$ | (-) |
| Dissipated energy in a load cycle | E_D | $6.8 \cdot 10^{-3}$ | $4.3 \cdot 10^{-2}$ | $1.5 \cdot 10^{-2}$ | $6.0 \cdot 10^{-4}$ | (kN/m ²) |
| Energy stored at maximum shear strain γ_c | E_S | $4.1 \cdot 10^{-3}$ | $2.0 \cdot 10^{-2}$ | $8.5 \cdot 10^{-3}$ | $8.5 \cdot 10^{-4}$ | (kN/m ²) |
| Maximum damping ratio (at maximum shear strain γ_c) | ξ | 13.1 | 17.1 | 14.0 | 5.6 | (%) |

The calculated global Factor of Safety is $\eta_{min} = 1.23$ without considering any dynamic effects.

The location of the dropped weight was varied along the slope system in different dynamic calculations (refer to Figure 10). Then, the resulting wave velocities were read out for each calculation at defined observation points (Figure 10, A through J) to ascertain the maximum impact on the slope stability. There was a considerable increase in the wave velocity recorded with dynamic compaction impacts at an interval of less than 30 m in front of the toe of slope. Figure 11 shows the horizontal wave velocity recorded with an impact 10 m in front of the toe of slope.

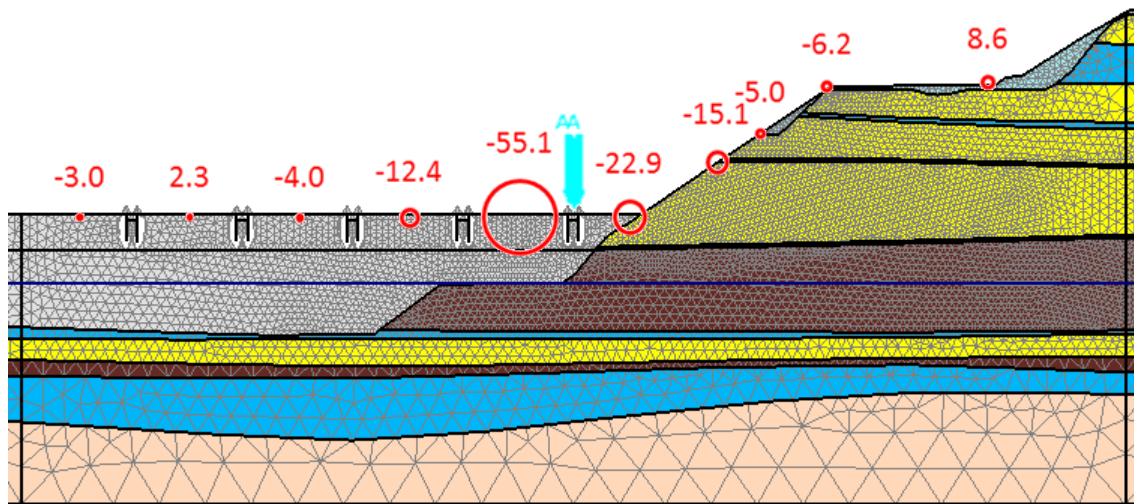


Figure 11 Recorded horizontal wave velocity with an impact 10 m in front of the toe of slope

The model allows analysis of the system (in this case, the slope) for each defined time increment of the dynamic calculations. The calculations were repeated while reducing the parameters $\tan \varphi'$ and c' until a continuous surface of connected zones of plastic failure points became apparent in one of the time increments. In these points the resistance shear strength is exceeded. Figure 12 shows a connection of failure points, which was indicated as the beginning of a slope failure. An impact 30 m in front of the toe of the slope was applied. The shear strength was reduced by a factor of $\gamma_{\varphi/c} = 1.15$.

Finally it was possible to demonstrate the required global stability of the overall system of $\eta_{req} = 1.10$ due to dynamic compaction within 12 m in front of the toe of the slope.

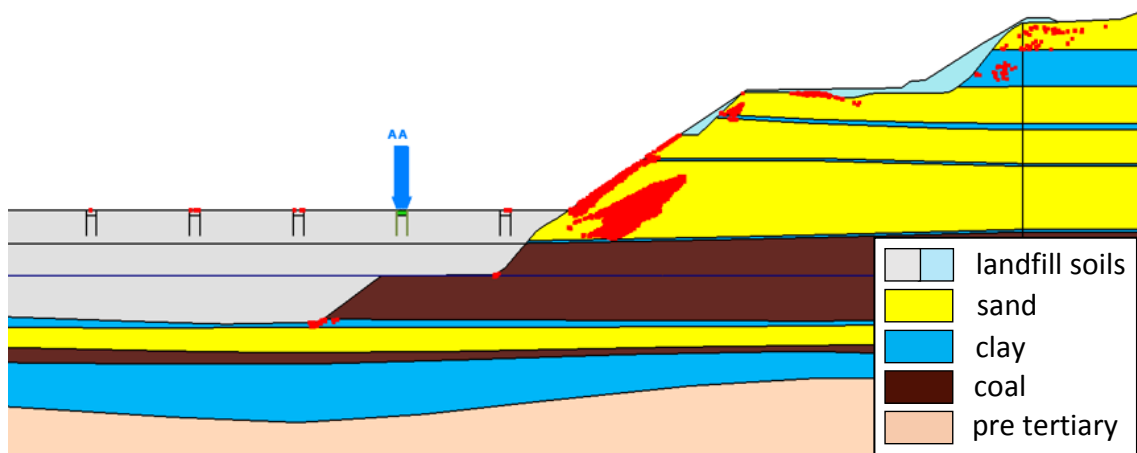


Figure 12 Evaluating the potential failure points (MC points) in connection with the dynamic effect for the reduction level $\gamma_{\varphi/c} = 1.15$

3 Dynamic compaction and the accompanying monitoring

The wave velocity limits were derived from the calculation at defined distances to the point of impact. They are presented in Table 4.

Table 4 Horizontal wave velocity limits during dynamic compaction $v_{h,req}$ depending upon the distance to the point of impact

| Distance to initial | (m) | 10 | 20 | 30 | 50 | 70 | 100 |
|---------------------|--------|----|----|----|-----|-----|-----|
| $v_{h,req}$ | (mm/s) | 50 | 30 | 15 | 9,5 | 6,5 | 5 |

A test field with accompanying vibration measurements was set up to confirm the model assumptions initially starting with the compression impacts outside of the area that had an influence on the stability of the slope. The test impacts were gradually brought up to the toe of the slope provided they do not exceed the specified limits for wave velocities. The test impacts were made at a reduced falling height from a distance of 12 m and the maximum amplitudes of the wave velocity were mechanically recorded. Figures 13 and 14 show the arrangement of the measuring points.

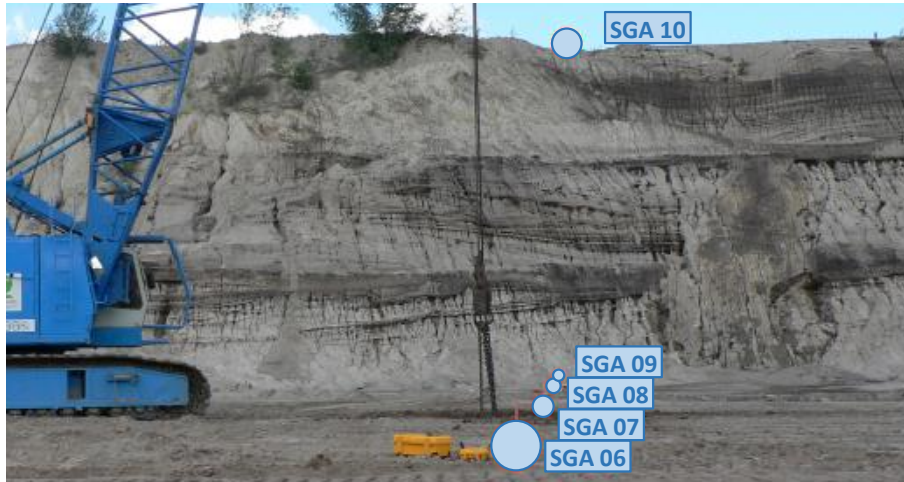


Figure 13 Vibration measurements on the solid border slope (modified from Geophysik GGD 2012)

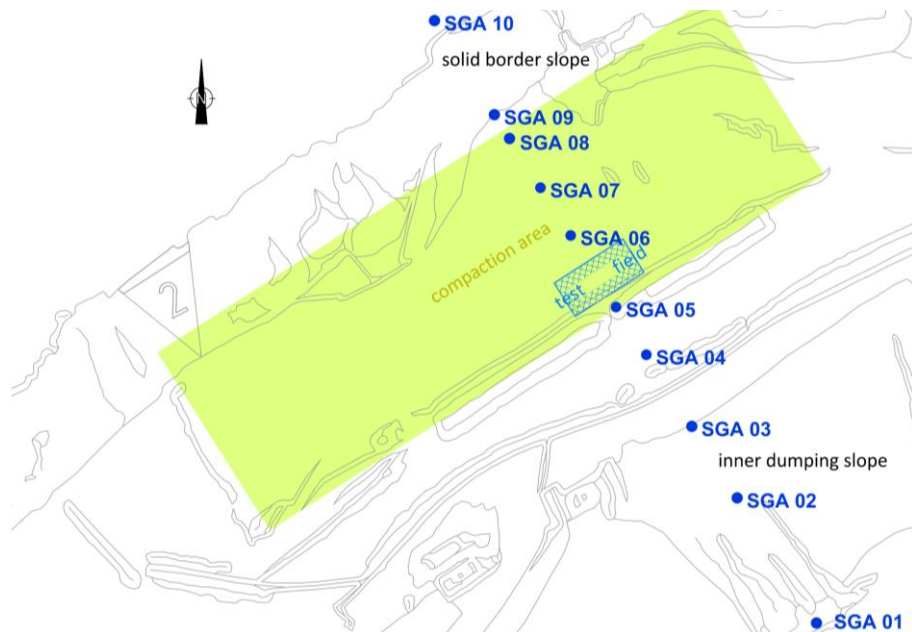


Figure 14 Ground plan for the SGA01 to SGA10 measuring points

Figure 15 shows the readings recorded in situ for various falling heights. In addition, the wave velocity defined as a limit is drawn as a curve at a radial distance to the initial shot according to Table 3.

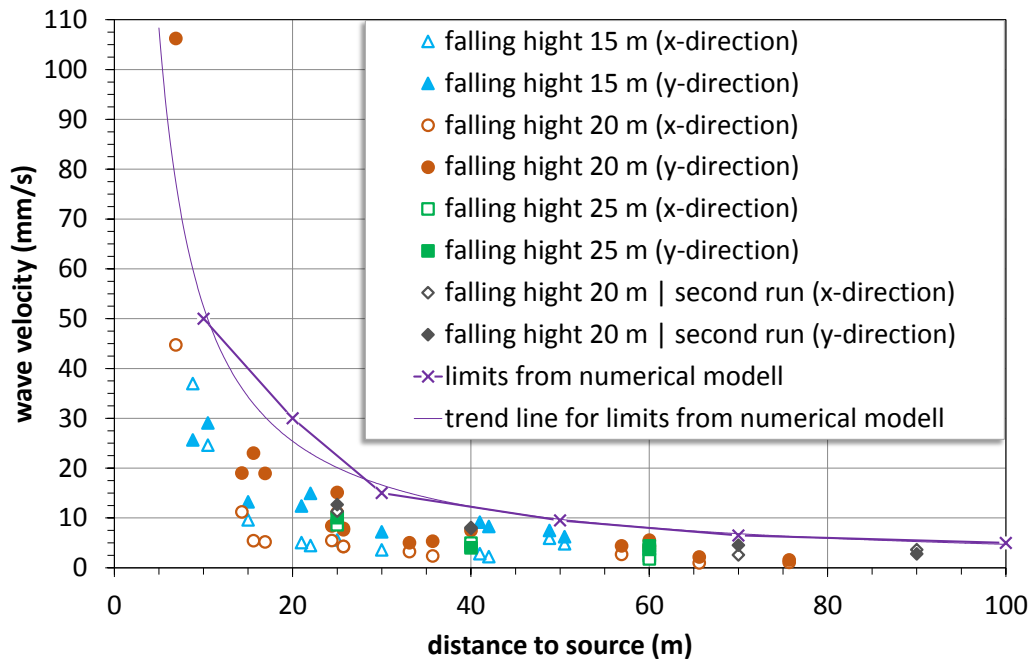


Figure 15 Readings of the wave velocity and defined limits

These measurements indicate that the system’s damping was recorded in the calculation with sufficient precision and the limits specified by the calculation in the test field were compiled appropriately. Therefore, the dynamic compaction was approved for implementation based on these findings and used in this fashion.

4 Conclusion

MIBRAG planned to build a mass distributor on a dump area in connection with expanding the working field at the Vereinigtes Schleenhain open pit mine. The mass distributor is a fully automated system which sorts the extracted brown coal and the overburden on different conveyor belts. Brown coal is then transported to a central coal stockyard, while overburden is transported to the dump area.

In order to improve the bearing capacity of the dumped soil, material densification was planned using dynamic compaction. The area to be improved was on the lower levels within the active open pit between a solid rim slope and an inner dump slope. The challenge was to use finite element modelling to discover whether the dynamic effects from the impact impulses from dynamic compaction had a destabilising impact on the slopes in an open pit operation.

Soils have been modelled using the hardening soil model with small strain stiffness which includes a hysteretic damping. Initial calculations showed that it was not possible to achieve any significant reduction in wave velocity in the initial set back distance of more than 30 m from dynamic impacts. As there is also damping in soils even if strains are very small, a Rayleigh damping was additionally defined.

To ascertain the maximum impact on the slope stability the location of the dropped weight was varied along the slope system under different dynamic calculations. There was a considerable increase in the wave velocity recorded with dynamic compaction impacts at an interval of less than 30 m in front of the toe of the slope.

To determine the Factor of Safety for the slope, dynamic calculations were repeated while reducing effective shear strength ($\tan \varphi'$ and c') until a continuous surface of connected plastic shearing, characterising a slope failure, became apparent. The Factor of Safety for the slope was determined by the ratio of shear strength at this observed failure to the available shear strength using Fellenius’s law (Fellenius 1936). Finally it was possible to prove the global stability of the overall systems of $\eta_{req} = 1.10$ required at a distance of dynamic compaction within 12 m of the toe of the slope.

A test field with accompanying vibration measurements was set up to confirm the model assumptions initially starting with the compression impacts outside of the area that had an influence on the stability of the slope. The test impacts were gradually brought up to the toe of the slope under the condition that they do not exceed the specified wave velocity limits. These limits were specified at defined distances to the impact point. The vibration measurements indicate that the system's damping was recorded in the calculation with sufficient precision and the limits specified by the calculation in the test field were compiled appropriately. Therefore, the dynamic compaction was approved for implementation based on these findings and used in this fashion.

The dynamic compaction was carried out successfully.

References

- Alpan, I 1970, 'Geotechnical properties of soils', *Earth-Science Reviews*, vol. 6, pp. 5–49.
- Benz, T 2007, 'Small strain stiffness of soils and its numerical consequences', PhD thesis, University of Stuttgart.
- Benz, T, Schwab, R & Vermeer, PA 2006, 'A small strain overlay model, I: model formulation', *International Journal for Numerical and Analytical Methods in Geomechanics*.
- Brinkgreve, RBJ, Kappert, MH & Bonnier, PG 2007, 'Hysteretic damping in a small-strain stiffness model', in Pande & Pietruszczak (eds), *Numerical Models in Geomechanics*, London.
- Darendeli, MB 2001, 'Development of a New Family of Normalized Modulus Reduction and Material Damping Curves', PhD thesis, Department of Civil Engineering, The University of Texas at Austin.
- Fellenius, WKA 1936, 'Calculation of the Stability of Earth Dams', in *Transactions of the Second Congress on Large Dams*, Washington DC, 4, pp. 445–462.
- Geophysik GGD mbH 2010, 'BV Ersatz der B 176, Dynamische Intensivverdichtung, Erschütterungsmessungen nach DIN 4150-3', Leipzig.
- Geophysik GGD mbH 2012, 'Geotechnischer Bericht: Tagebau Vereinigtes Schleenhain, Abbaufeld Peres, Bauvorhaben Errichtung eines Massenverteilers, Dynamische Intensivverdichtung, Erschütterungsmessungen nach DIN 45669', Leipzig.
- Kirstein, JF & Krings, M 2012, 'Dynamische Intensivverdichtung am Bestand - mehr als 30 Jahre Erfahrung - Schwingungsmessungen und neue Entwicklungen', *Tagungsband zur achten Erdbaufachtagung*, Leipzig.
- Peterie, SL, Miller, RD & Ivanov, J 2014, 'Seismology and its Applications in Kansas', *Kansas Geological Survey, Public Information Circular 37*, The University of Kansas at Lawrence.
- Plaxis 2015, *PLAXIS 2015: Material Models Manual*, Delft University of Technology & Plaxis b.v.
- Schanz, T, Vermeer, PA & Bonnier, PG 1999, 'Formulation and verification of the Hardening-Soil Model', in RBJ Brinkgreve (ed.), *Beyond 2000 in Computational Geotechnics*, Balkema, Rotterdam, pp. 281–290.
- Woods, RD 1968, 'Screening of surface waves in soils', *Journal of the Soil mechanics and Foundation Division*, ASCE, vol. 94, no. SM4, pp. 951–979.

